Study on POD Analysis and Reduced-Order Modeling of Fluctuating Wind Pressure on Large-Span Cantilever Canopy Roofs From the Perspective of Spatiotemporal Evolution Characteristics

Yongtao Bai* and Qiteng Zhao

School of Civil Engineering, Chongqing University, Chongqing 400045, China

Abstract: This study investigates the spatiotemporal evolution of fluctuating wind pressure on large-span cantilever canopy roofs under complex wind fields. Employing Proper Orthogonal Decomposition (POD), we perform modal decoupling and energy distribution analyses on high-dimensional pressure time-history data from 32 measurement points of a 48m×96m large-span cantilever canopy roof. Results show that the first-order mode displays strong global coherence, contributing 32.41% of the total energy. With increasing mode order, the spatial structure transitions from global patterns to local vortex features; the first ten modes collectively account for 78.11% of the total energy, capturing the edge flow separation and multi-scale vortex shedding behaviors of the rectangular cantilever structure. Signal reconstruction at key windward points verifies that the low-dimensional POD model enhances computational efficiency while preserving the dynamic features of the original flow field, thereby offering theoretical support for wind-resistant design of large-span structures and compression of structural monitoring data.

Keywords: Large-span cantilever canopy roof, Proper Orthogonal Decomposition, Fluctuating wind pressure field, Spatiotemporal evolution characteristics, Energy distribution characteristics.

1. INTRODUCTION

With the rapid development of high-strength material technology and innovations in structural forms, large-span cantilever canopy roofs have been widely applied in engineering scenarios such as large stadiums, transportation hubs, and exhibition centers, emerging as typical representatives of modern large-span structures. Characterized by lightweight, high flexibility, and low damping, such structures are extremely sensitive to dynamic excitations induced by wind loads. Unlike enclosed buildings with relatively stable flow fields, the airflow around cantilever canopy roofs exhibits strong unsteady flow characteristics: intense flow separation occurs when airflow passes the windward edge, triggering complex vortex shedding and multi-scale coherent structures [1-4]. Furthermore, the aspect ratio (length-to-width ratio) of the roof significantly regulates the spatiotemporal correlation of the surface pressure field, ultimately resulting in an asymmetric and highly random fluctuating wind pressure distribution. These aerodynamic characteristics pose prominent challenges to the wind-resistant design and structural safety assessment of such engineering structures [5-7].

Wind load analysis of large-span cantilever structures has long been a persistent research focus in wind engineering. Traditional analytical methods rely heavily on mean wind pressure distributions and statistics of local peak fluctuations, with their core limitation lying in the dependence on single-point measurement data—making it difficult to reveal the spatiotemporal evolution mechanism and coherence characteristics of the pressure field. Such methods overlook the intrinsic correlations and temporal synchronization of pressure fluctuations at different spatial points, resulting in design parameters that fail to accurately reflect the actual dynamic responses of structures under complex wind environments and thus diminishing the reliability of their engineering applications [8-12].

Proper Orthogonal Decomposition (POD), an energy-optimized mathematical transformation method, has emerged as a core tool for extracting coherent structures from complex random fields [13-15]. This method decomposes the fluctuating wind pressure field into orthogonal spatial modes and uncorrelated temporal principal coordinates, enabling accurate mapping of high-dimensional time-series data to low-dimensional physical models—a unique advantage that has led to its widespread application in wind pressure analysis of building structures. Y. Tamura *et al*. [16] employed wind tunnel tests and POD to analyze the correlation between fluctuating wind pressure on low-rise buildings and the oncoming flow. They found that the error of wind pressure reconstruction using the first 10 or more POD modes can be controlled within 3%, with the first and second wind pressure modes correlating with the longitudinal (u) and lateral (v) components of the oncoming flow, respectively. They

*Address correspondence to this author at the School of Civil Engineering, Chongqing University, Chongqing 400045, China;
E-mail: bai.yongtao@cqu.edu.cn

Received on 31-12-2025 Accepted on 10-02-2026 Published on 18-02-2026

E-ISSN: 3110-9780/26

also indicated that the upstream wind speed at building height is not necessarily the optimal reference wind speed for wind pressure research. Subsequently, they further explored the application of POD in analyzing random fluctuating wind pressure fields on building surfaces, clarifying key considerations such as the need to exclude mean components and account for singular conditions [17]. Through wind tunnel tests on high-rise buildings, they verified that POD can effectively extract hidden systematic structures from random fluctuations, significantly reduce data volume, and accurately reconstruct wind loads and building wind responses based on a small number of dominant modes—providing critical support for reduced-order modeling. Byungryul Kim and K.T. Tse [18] conducted wind tunnel tests on two linked high-rise buildings with different spacings. They used POD to identify hidden pressure patterns, investigate their aerodynamic characteristics and inter-building aerodynamic correlations, and combined Dual Modal Transformation (DMT) to analyze the influence of POD modes on structural modes. Meanwhile, they studied the role of structural connections and found that connections can significantly reduce wind-induced responses under negative aerodynamic correlation, but have no obvious effect under positive correlation. Lei Zhou *et al*. [19] simulated twisted wind profiles (TWP) with different maximum twist angles (15°, 30°) in a wind tunnel using an adjustable wooden blade system, and conducted surface pressure tests on rectangular high-rise buildings at various angles of attack (-90° to 90°). Combining POD, they extracted the spatiotemporal and spectral characteristics of pressure patterns, and compared with conventional wind profiles (CWP) to explore the influence of TWP on building aerodynamic forces and global/local correlations. They found that TWP alters the offset angle of aerodynamic force curves, amplifies mean torsional forces, suppresses vortex shedding, and enhances force component correlations—with the intrinsic mechanism of its impact on aerodynamic characteristics rooted in changes in pressure patterns. Kuiwen Yuan *et al*. [20] proposed a novel reduced-order model integrating POD and Higher-Order Dynamic Mode Decomposition (HODMD). Through wind tunnel tests and Large Eddy Simulation (LES), they investigated the aerodynamic interference and flow field mechanisms of three-dimensional finite-length tandem square cylinders, revealing that structural spacing modifies the separation and reattachment positions of shear layers as well as pressure distribution. Low-frequency and high-frequency modes respectively affect gap vortex distribution and vortex continuity, while vortex shedding modes enhance the development of separated vortices and wake vortices. Additionally, the model effectively establishes the correlation between frequency, mode, and energy. However, existing POD-related studies have mostly focused on enclosed buildings, symmetric cantilever structures with small aspect ratios (*e.g*., 1:1 or 1:1.5), or isolated components. Systematic POD analysis and reduced-order modeling research on fluctuating wind pressure fields of large-span cantilever canopy roofs with asymmetric aspect ratios (*e.g*., 2:1) remain relatively scarce. For the 48m×96m large-span cantilever canopy roof with a 2:1 aspect ratio studied in this paper, flow separation at its edges is more intense, and the interaction between multi-scale vortices is more complex—resulting in significant differences in the spatiotemporal evolution characteristics of its fluctuating wind pressure field compared to traditional symmetric structures. Recent studies have shown that the POD modal energy distribution of such asymmetric large-span cantilever structures is often more dispersed, and existing conclusions based on symmetric structures cannot fully explain this phenomenon. Furthermore, the academic community currently lacks in-depth analysis of the topological characteristics of dominant POD modes of such structures and their intrinsic correlations with actual flow phenomena (*e.g*., vortex shedding frequency, flow separation position), which greatly hinders the accurate understanding of the mechanism of wind-induced dynamic responses of such structures. Therefore, conducting systematic POD analysis and reduced-order modeling research on large-span cantilever canopy roofs with a 2:1 aspect ratio holds important theoretical significance and engineering application value.

This study takes a 48m×96m large-span cantilever canopy roof as the research object and employs Proper Orthogonal Decomposition (POD) to conduct systematic analysis on synchronous pressure time-series data from 32 measurement points. The specific research objectives are as follows: (1) extract the dominant spatial modes of the fluctuating wind pressure field and reveal their topological characteristics and spatiotemporal evolution laws; (2) quantify the energy distribution characteristics of each POD mode and explore the intrinsic mechanism underlying the dispersed energy distribution of the target structure; (3) verify the accuracy and reliability of the low-dimensional POD model through pressure signal reconstruction at key measurement points and evaluate its engineering application value. The research results are expected to provide theoretical support and engineering reference for the wind-resistant design, reduced-order dynamic analysis, and data compression in structural health monitoring of large-span cantilever structures, as well as offer insights for the design and research of similar projects.

2. METHODOLOGY

2.1. Overview of Research Data

The object of this study is a large-span cantilevered canopy roof with planar dimensions of 48m×96m. The wind pressure data used in this analysis were obtained from a series of high-precision wind tunnel tests conducted on a scaled model, provided for this research through authorized datasets. The experiments were performed in a boundary layer wind tunnel, where the incoming flow was conditioned to simulate the characteristics of a typical atmospheric boundary layer.

The target structure features a typical asymmetric configuration with a 2:1 aspect ratio. The design adopts a low-rise cantilevered form, incorporating a modest inclination that maintains the streamlined aerodynamic profile of the canopy while reflecting the functional requirements of large-span structures. To isolate the fundamental aerodynamic mechanisms, the structure is modeled in an isolated boundary condition, free from the interference of surrounding building clusters. This setup allows the analysis to focus on the intense flow separation at the windward edge and the multi-scale vortex shedding across the roof surface.

The experimental setup, including the planar dimensions, the distribution of 32 synchronous measuring points, and the incoming wind direction, is schematically illustrated in Figure **1**. These measuring points were arranged in a global matrix of 4 columns along the x-direction (width) and 8 rows along the y-direction (length) to capture the spatiotemporal evolution of the pressure field. The total data sampling duration lasted 210s with a sampling interval of 0.07s, providing 3000 sample points per sensor. To ensure the universality of the results and to eliminate the influence of specific wind speeds or geometric scales, all original pressure data were converted into dimensionless pressure coefficients based on the dynamic pressure at the reference height. This normalization allows the Proper Orthogonal Decomposition (POD) analysis to focus specifically on the intrinsic spatiotemporal correlation and energy distribution of the fluctuating wind pressure field.

2.2. POD Analysis Method

To reveal the dominant spatial structure of the fluctuating pressure field, a standard data normalization and preprocessing procedure is applied. Prior to the modal decomposition, the raw pressure data are converted into dimensionless wind pressure coefficients to eliminate the influence of wind speed and scale. Let $P_{raw,i}(t)$ be the instantaneous pressure measured at point *i*. The dimensionless pressure coefficient $p_i(t)$ is defined as:

$$p_i(t) = \frac{P_{raw,i}(t) - P_\infty}{\frac{1}{2}\rho U_H^2} \tag{1}$$

where P_∞ is the static reference pressure and $\frac{1}{2}\rho U_H^2$ represents the dynamic pressure at the reference height. For the sake of mathematical consistency in the following steps, $p_i(t)$ is used to denote these normalized coefficients.

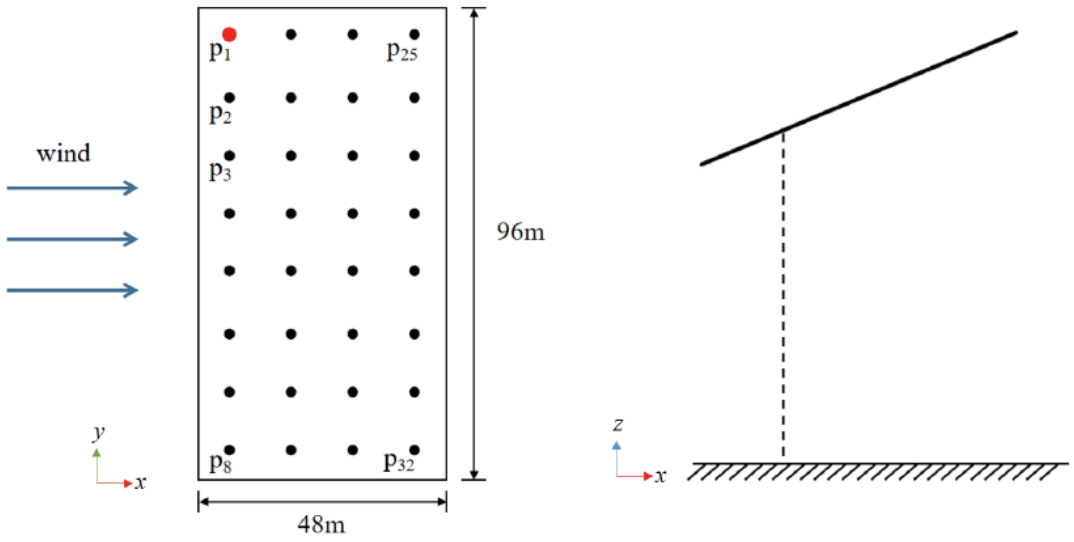

(**a**) (**b**)

Figure 1: Schematic diagram of the plan layout and vertical section of the large-span cantilever canopy roof. (**a**) Plan view of the cantilever canopy roof (including measurement point arrangement and incoming wind direction); (**b**) Schematic diagram of the vertical section of the cantilever canopy roof.

The core of the preprocessing involves the removal of the time-averaged component. For the *i*-th point (*i*=1,2,…,32) and the *t*-th time step (*t*=1,2,…,3000), the time-averaged pressure $\bar{p}_i$ is calculated as follows:

$$\bar{p}_i = \frac{1}{n}\sum_{t=1}^{n} p_i(t) \tag{2}$$

where *n*=3000 is the total number of samples for each measuring point.

Correspondingly, the fluctuating pressure component $\bar{p}_i$ is defined as the difference between the instantaneous pressure and the time-averaged pressure, and its expression is:

$$p_i'(t) = p_i(t) - \bar{p}_i \tag{3}$$

Based on the fluctuating pressure components of all measuring points, the covariance matrix $C \in \mathbb{R}^{32\times32}$ of the fluctuating pressure field is constructed. Its element C_{ij} is defined as the covariance of the fluctuating pressures, and the expression is:

$$C_{ij} = \frac{1}{n}\sum_{t=1}^{n} p_i'(t)\cdot p_j'(t) \tag{4}$$

Solve the following eigenvalue problem for the covariance matrix C:

$$C\phi_m = \lambda_m \phi_m \tag{5}$$

After solving, 32 eigenvalues λ_m (*m*=1,2,…,32) and corresponding eigenvectors ϕ_m can be obtained. Among them, the eigenvector ϕ_m corresponds to the m-th POD spatial mode, which reflects the spatial distribution characteristics of this mode across the 32 measuring points. Based on the above steps, POD analysis will be carried out on the fluctuating wind pressure field of the large-span cantilevered canopy roof in subsequent sections, to extract its dominant spatial structure and energy distribution characteristics.

3. RESULTS AND DISCUSSION

3.1. Topological Characteristics of Spatial Modes

The eigenvalues and eigenvectors were computed using MATLAB. The spatial distributions are plotted in Figures **1**, **2** and **3**.

Each ϕ_m represents the relative spatial pattern of the *m*-th pressure mode. For example, the 1st mode captures the most energetic, large-scale pressure fluctuation across the roof, while higher modes capture more localized variations.

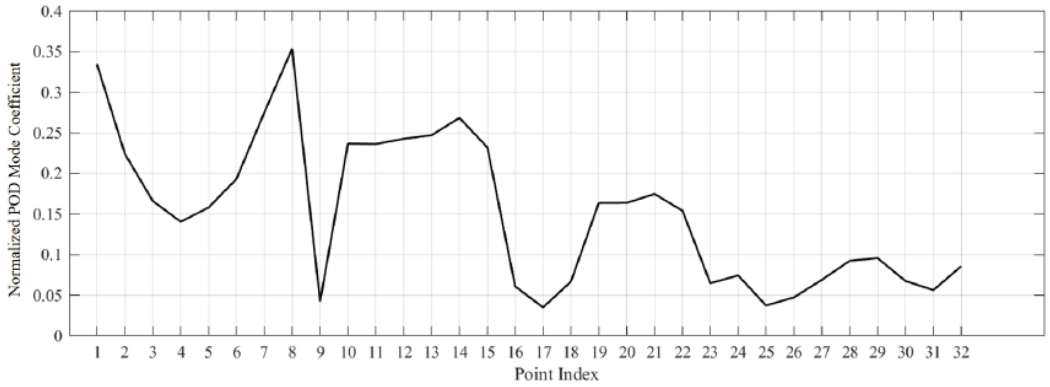

Figure 2: Spatial distribution of the 1st mode (line plot).

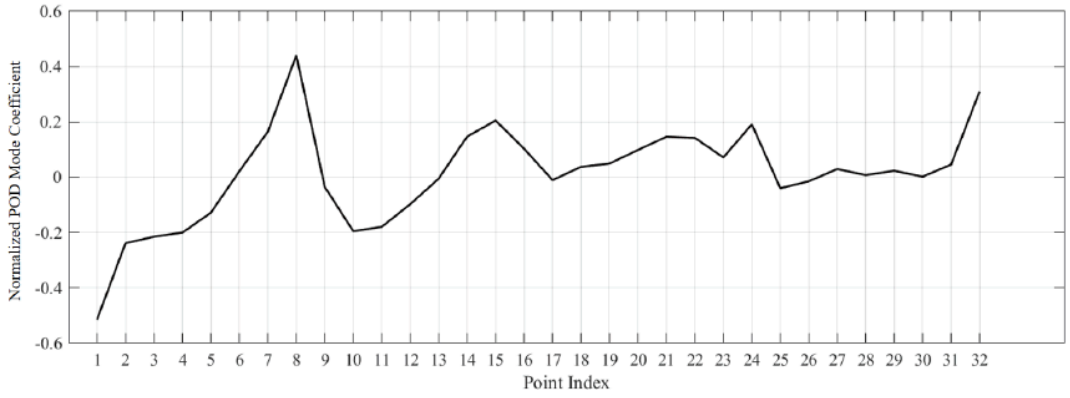

Figure 3: Spatial distribution of the 2nd mode (line plot).

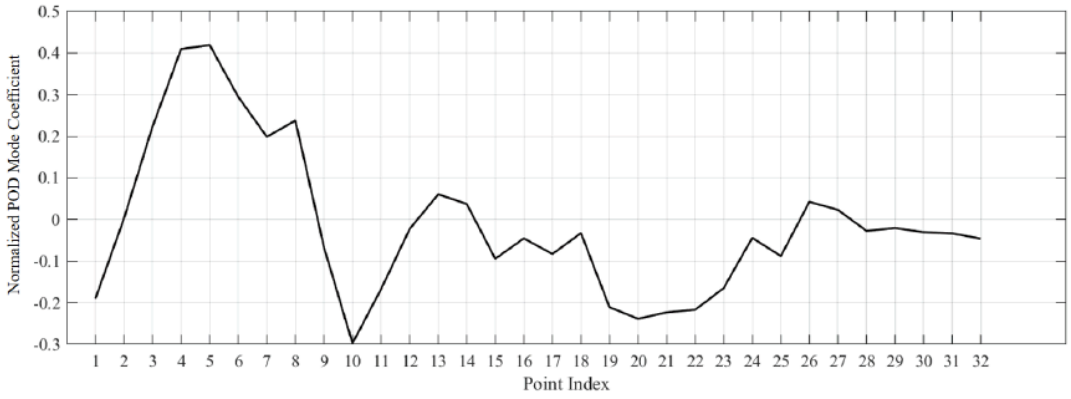

Figure 4: Spatial distribution of the 3rd mode (line plot).

In addition to the line plots of modal coefficients, the spatial distributions of the first three POD modes in the physical space are presented in Figure **5**(**a-c**). These contour plots provide a detailed visualization of how pressure patterns vary spatially across the roof surface in the x–y plane.

Specifically, Figure **5**(**a**) displays the 1st mode $\phi_1(x,y)$, which reflects the dominant pressure distribution characterized by a smooth and globally coherent pattern, representing the overall mean structural response to wind loading. Figure **5**(**b**) shows the 2nd mode $\phi_2(x,y)$, revealing a secondary pattern with increased spatial complexity and partial asymmetry, typically associated with localized flow separation or directional turbulence. Figure **5**(**c**) illustrates the 3rd mode $\phi_3(x,y)$, which captures high-frequency pressure fluctuations and finer-scale vortical features.

These spatial mode shapes not only complement the temporal analysis but also provide physical insights into how energy is distributed across the surface. Understanding such patterns is essential for identifying critical pressure zones and optimizing structural form for wind resistance in practical engineering design.

Overall, the first three modes already capture significant spatial characteristics of the fluctuating pressure field. This indicates that a large portion of the physically meaningful information is concentrated in the leading modes, making them suitable for use in simplified representations.

The effectiveness of this modal decomposition provides a solid foundation for reduced-order modeling, which can greatly improve computational efficiency in subsequent simulations. Furthermore, these dominant modes can serve as basis functions for reconstructing pressure fields, enabling accurate approximation of the original data while minimizing dimensional complexity. Such an approach is particularly beneficial in structural wind engineering, where efficient yet accurate modeling is essential for performance evaluation, design optimization, and control strategy development.

The topological features of the POD modes are intrinsically linked to the underlying aerodynamic mechanisms of the large-span cantilevered structure. The 1st mode ϕ_1, which exhibits strong global coherence and accounts for 32.41% of the total energy (as detailed in Section 3.2), is primarily driven by quasi-static pressure fluctuations associated with the

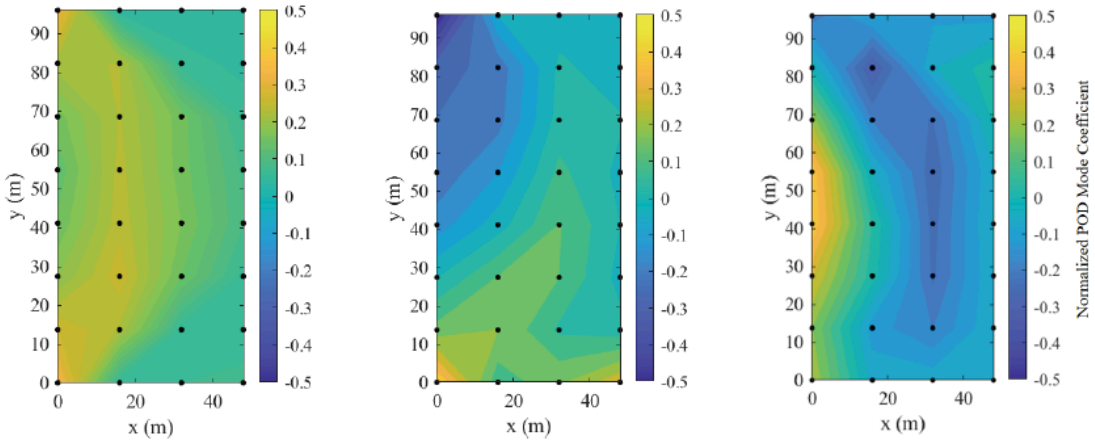

(**a**) (**b**) (**c**)

Figure 5: Spatial distribution of the first three POD modes in x–y plane: (**a**) 1st mode; (**b**) 2nd mode; (**c**) 3rd mode.

large-scale turbulence of the oncoming flow. In contrast, the higher-order modes (ϕ_3, ϕ_3) represent the physical manifestations of flow separation at the windward edge and subsequent vortex shedding over the roof surface. While the modest inclination of the canopy helps maintain a streamlined aerodynamic profile, the sharp windward edge remains a critical source of unsteady multi-scale vortical structures. A qualitative spectral analysis of the principal coordinates $a_m(t)$ further supports this interpretation. The Power Spectral Density (PSD) of $a_1(t)$ is dominated by low-frequency energy, consistent with the global structural response, whereas the spectra of higher modes are expected to exhibit distinct energy peaks aligned with the Strouhal frequency of periodic vortex shedding. This confirms that the POD method effectively extracts dominant dynamic features from the complex fluctuating pressure field.

However, spatial modes only reflect the "static distribution characteristics" of the pressure field. To fully describe the spatiotemporal evolution law of the fluctuating pressure field, it is also necessary to clarify the law of excitation variation of each mode with time, which is precisely characterized by the principal coordinates. The principal coordinates $a_m(t)$ describe how each spatial mode ϕ_m is excited over time. Let the principal coordinates be computed as:

$$a_m(t) = \sum_{i=1}^{32} \phi_{m,i} \cdot p_i'(t), \quad m = 1,2,3 \tag{6}$$

where: $\phi_{m,i}$ is the *i*-th component of the *m*-th eigenvector ϕ_m, $p_i'(t)$ is the fluctuating pressure at point *i* and time *t*, as defined in 3.1.

Alternatively, the computation can be written in matrix form as:

$$\{a\}(t) = [\phi] \quad \{p'(t)\} \tag{7}$$

The temporal variations of the first three principal coordinates $a_1(t)$, $a_2(t)$ and $a_3(t)$ were obtained using MATLAB. The full time histories of $a_1(t), a_2(t)$ and $a_3(t)$ are shown in Figures **6**, **7** and **8**, respectively. A combined comparison of these three principal coordinates is provided in Figure **9**. Figure **9** reveals that the 1st mode is strongly excited with larger amplitude fluctuations, indicating its dominant energy content. Figure **7** and Figure **8** show smaller yet non-negligible excitations of the 2nd and 3rd modes. Figure **9** illustrates the overall comparative behavior among the first three principal coordinates over time.

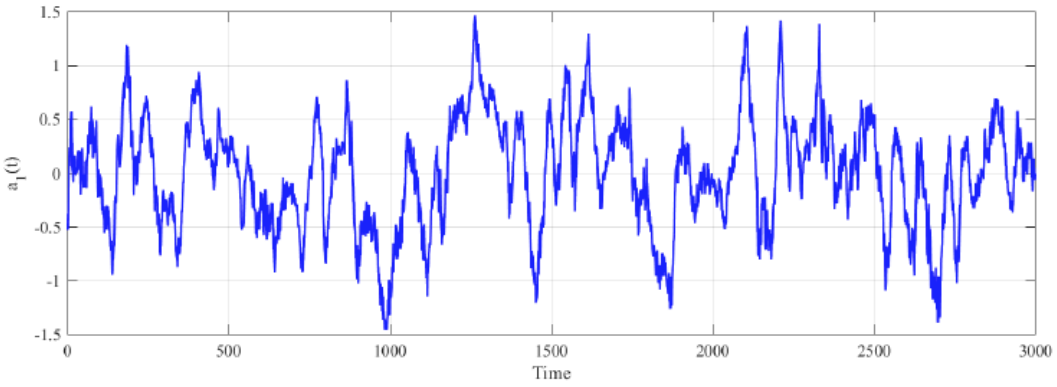

Figure 6: Principal Coordinate $a_1(t)$ of 1st Mode.

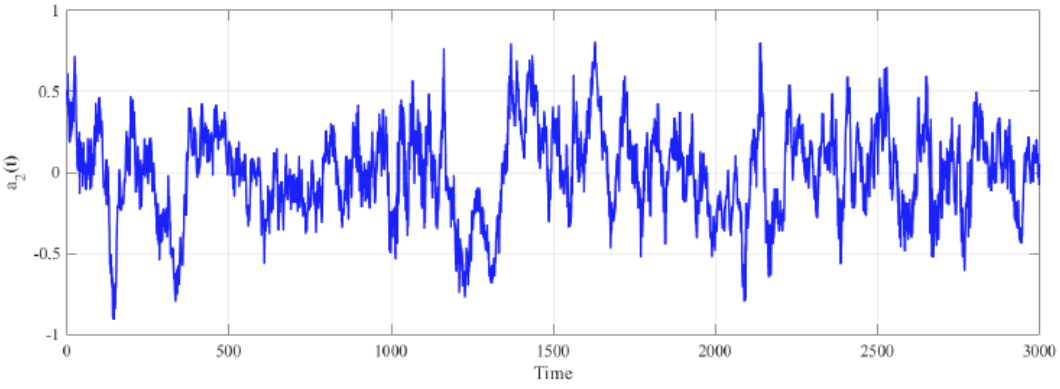

Figure 7: Principal Coordinate $a_2(t)$ of 2nd Mode.

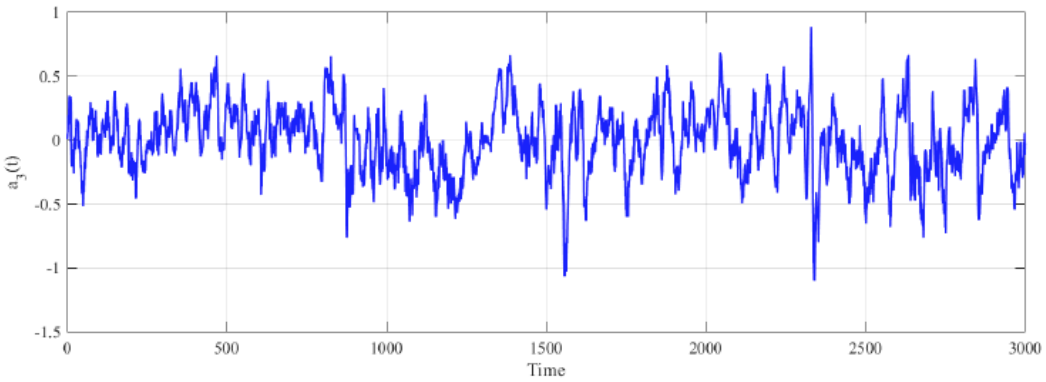

Figure 8: Principal Coordinate $a_3(t)$ of 3rd Mode.

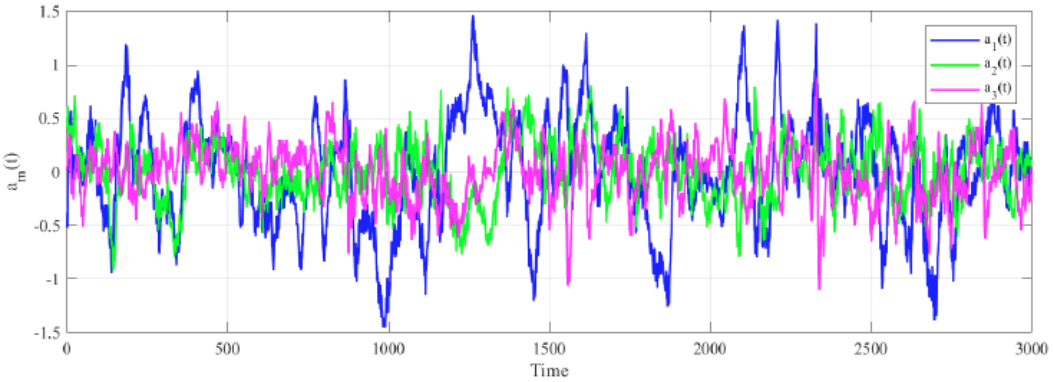

Figure 9: Comparison of $a_1(t)$, $a_2(t)$, and $a_3(t)$

3.2. Energy Distribution Laws of Modes

The eigenvalue λ_m ecorresponding to each mode reflects the energy content in that mode, the variance contribution of the pressure field along the direction of the corresponding eigenmode. The energy proportion of each mode is defined as $\sum_{m=1}^{32}\lambda_m$.

The energy contribution of the *m*-th mode is expressed as:

$$c_m = \frac{\lambda_m}{\sum_{i=1}^{32}\lambda_i} \times 100\% \tag{8}$$

The cumulative energy contribution up to the *N*-th mode is:

$$C_N = \sum_{m=1}^{N} c_m \tag{9}$$

Using MATLAB, the eigenvalues and their

Table 1: Proportion and Cumulative Proportion of the First 10 Modes

Mode	Eigenvalue λ_m	Proportion c_m(%)	Cumulative Proportion C_N(%)
1st	0.26089	32.41	32.41
2nd	0.07625	9.47	41.88
3rd	0.06975	8.66	50.54
4th	0.05390	6.69	57.24
5th	0.03957	4.92	62.15
6th	0.03355	4.17	66.32
7th	0.02733	3.39	69.71
8th	0.02637	3.28	72.99
9th	0.02128	2.64	75.63
10th	0.01996	2.48	78.11

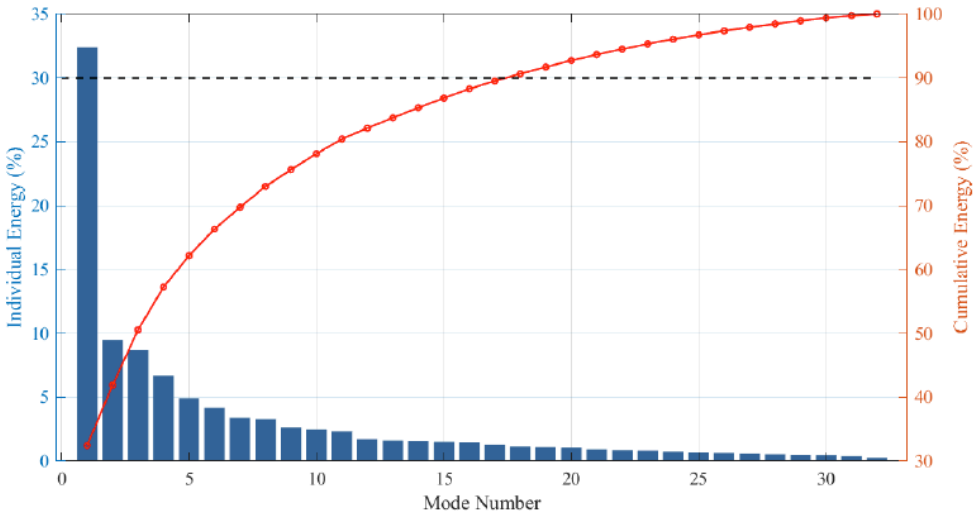

Figure 10: Individual and cumulative energy contribution of POD modes.

proportions were computed, and the results for the first 10 modes are listed in Table **1**.

The individual and cumulative energy distributions are visualized in Figure **10**, showing the contribution of each mode in descending order of significance. The energy distribution among the modes in this study is notably dispersed, reflecting the inherent complexity of the pressure field. As shown in Table **1**, the first 10 modes contribute 78.11% of the total energy. As illustrated by the cumulative energy curve, the 90% energy threshold is reached at the 18th mode. This relatively slow decay rate is a distinct departure from smoother or more symmetric structural flows where 90% of the energy is often concentrated in fewer than 10 modes.

Such energy dispersion is not a limitation of the POD method, but rather a physical indicator of the multi-scale turbulent interactions over the 2:1 aspect ratio canopy. The intense flow separation and randomized vortex shedding at the asymmetric edges introduce significant energy into higher-order modes. Therefore, instead of seeking an arbitrary 90% threshold, this study focuses on the dominant modes that capture the primary spatiotemporal evolution. The results demonstrate that the first 10 modes are sufficient to represent the core physical features of the pressure field, while the "long tail" of the energy spectrum confirms the highly chaotic and multi-modal nature of the flow.

3.3. Verification of Signal Reconstruction for the Low-Dimensional POD Model

The distribution characteristics of the modal components of each order corresponding to Point 1 can be intuitively reflected in Figure **11**. This figure shows the proportion of coefficients of the first three modes at Point 1, clearly revealing the differences in the contribution weights of different-order modes to the pressure signal at this point. It also provides an intuitive basis for the subsequent selection of the first *N*=1, 2, 3 modes for reconstruction.

To evaluate the effectiveness of modal decomposition, the fluctuating pressure at Point 1, $\hat{p}_1(t)$, is reconstructed using the lowest *r*=1,2,3 modes. The reconstruction is expressed as:

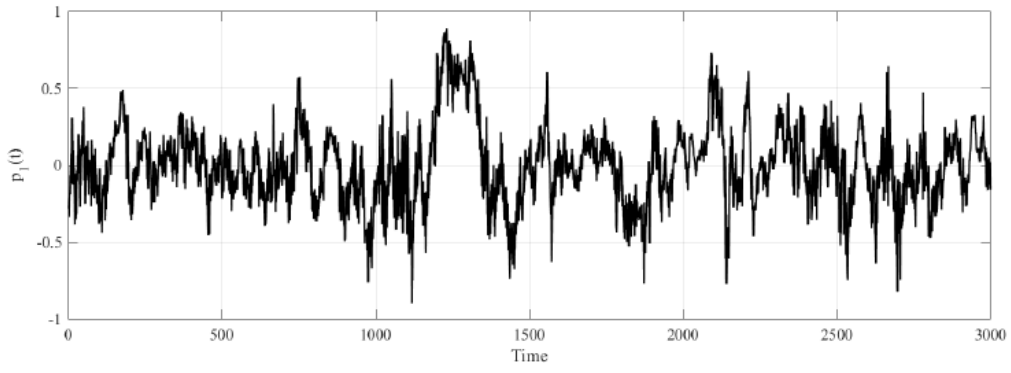

Figure 11: Original wind pressure signal $\hat{p}_1(t)$ at Point 1.

$$\hat{p}_i(t) \approx \sum_{m=1}^{r} \phi_{m,i} \cdot a_m(t) \tag{10}$$

For this case:when r=1 (1st mode only), $\hat{p}_1(t) = 0.33437 \cdot a_1(t)$;when r=2 (up to 2nd mode), $\hat{p}_1(t) = 0.33437 \cdot a_1(t) - 0.51457 \cdot a_2(t)$; when r=3 (up to 3rd mode), $\hat{p}_1 = 0.33437 \cdot a_1(t) - 0.51457 \cdot a_2(t) - 0.18960 \cdot a_3(t)$.

The time series of the reconstructed pressure signal was computed using MATLAB. The reconstruction results are visualized in Figures **12**, **13** and **14**, each showing the reconstructed signal using the first r=1, r=2, and r=3 modes, respectively. Figure **15** directly compares the original pressure signal at Point 1 with the signal reconstructed using the first three modes.

As shown in Figure **15**, the reconstructed signal using the first three modes closely follows the original time series in both trend and amplitude. This confirms that the dominant characteristics of the pressure field can be effectively captured using only a few modes. This significantly reduces the dimensionality of the system while preserving essential physical information, which is beneficial for real-time data compression, structural health monitoring, or reduced-order modeling.

To objectively evaluate the accuracy of the low-dimensional reconstruction, two quantitative metrics are introduced: the root-mean-square error ($RMSE$) and the normalized root-mean-square error ($NRMSE$). These metrics are defined as follows:

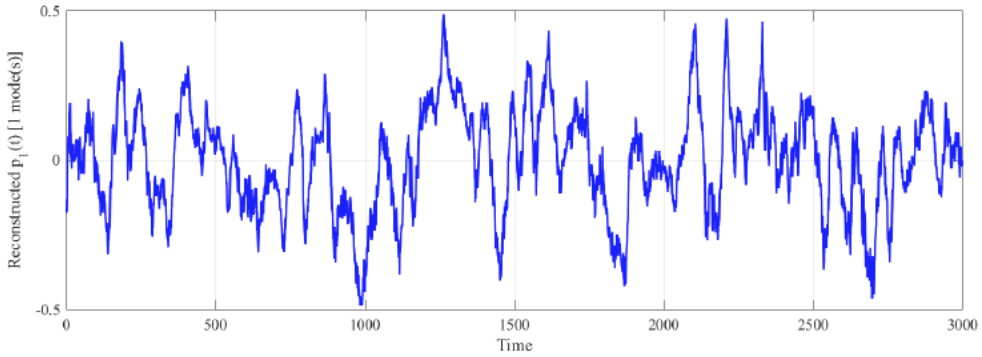

Figure 12: Reconstructed $\hat{p}_1(t)$ using only the 1st mode.

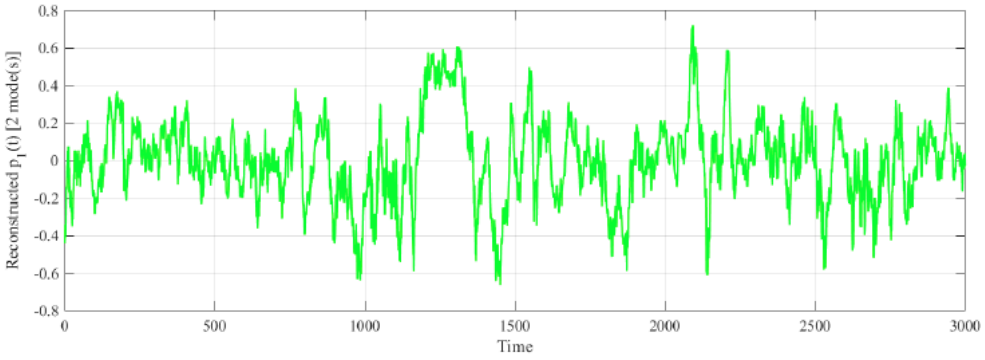

Figure 13: Reconstructed $\hat{p}_1(t)$ using the 1st and 2nd modes.

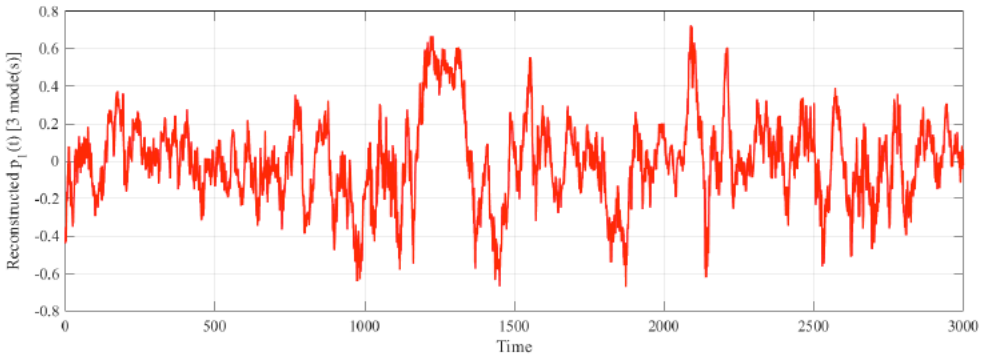

Figure 14: Reconstructed $\hat{p}_1(t)$ using the 1st to 3rd modes.

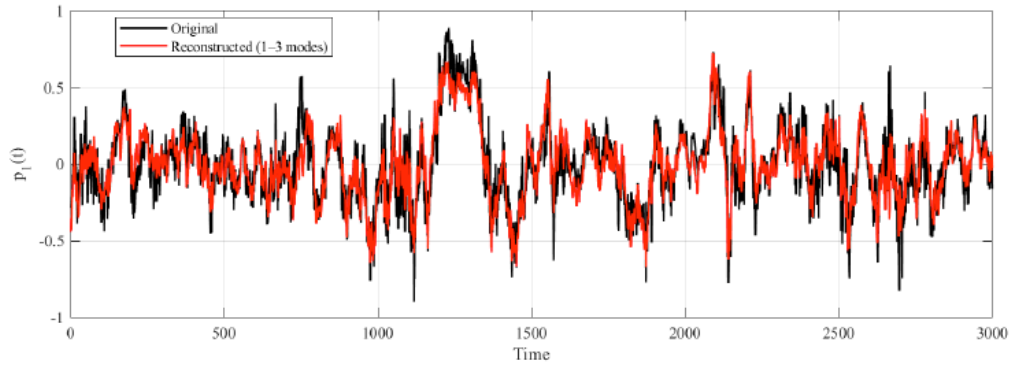

Figure 15: Comparison between original and reconstructed $\hat{p}_1(t)$ using 3 modes.

$$RMSE = \sqrt{\frac{1}{N}\sum_{t=1}^{N}\left(p(t)-\hat{p}(t)\right)^2} \tag{11}$$

This metric quantifies the average magnitude of the reconstruction error between the original fluctuation signal $p(t)$ and the reconstructed signal $\hat{p}(t)$, where *N* represents the total number of time samples in the fluctuating pressure signal.

$$NRMSE = \frac{RMSE}{p_{\max} - p_{\min}} \times 100\% \tag{12}$$

This metric normalizes the $RMSE$ by the peak-to-peak range (full scale) of the original fluctuation signal, providing a dimensionless measure of the relative reconstruction precision. Here, $p_{\max}$ and $p_{\min}$ denote the maximum and minimum values of the original pressure signal, respectively.

The validation is focused on the windward corner (Point 1), which represents the most aerodynamically complex region with intense flow separation in urban rail transit or civil engineering structures. As shown in Figure **15**, the reconstructed signal $\hat{p}(t)$ using the first three modes matches the original signal $p(t)$ with high fidelity. The $RMSE$ is 0.1105 and the $NRMSE$ is 6.18%, proving that the primary aerodynamic features are effectively captured.

3.4. Limitations and Future Perspectives

While the proposed POD-based framework demonstrates high efficiency in characterizing and reconstructing the fluctuating wind pressure, several limitations should be acknowledged to define the scope of the current study.

(1) The current analysis is based on a single cantilevered geometry with a 2:1 aspect ratio under a specific wind direction. In actual engineering scenarios, the aerodynamic response may vary significantly with different structural configurations and wind angles. Future research will focus on extensive parametric studies to evaluate the framework's robustness under diverse wind conditions.

(2) The pressure field was characterized using 32 measurement points. Although this resolution is sufficient for capturing the dominant load features as demonstrated by the 6.18% *NRMSE*, it may not fully resolve the finest scales of turbulence in the "long-tail" region of the energy spectrum. Increasing the sensor density or integrating the experimental data with high-fidelity Computational Fluid Dynamics (CFD) or Large Eddy Simulation (LES) results through data fusion techniques will be a key direction for future work.

(3) Current validation is primarily experimental. Cross-validation with high-fidelity numerical simulations and testing on aerospace-specific models will further enhance the scientific rigor and broaden the applicability of the model to aero-thermo-fluid systems.

4. CONCLUSION

In this study, Proper Orthogonal Decomposition (POD) was applied to analyze the fluctuating wind pressure field on a cantilevered canopy roof. The proposed framework successfully achieved dimensionality reduction and feature extraction, providing a high-fidelity representation of complex aerodynamic loads. The specific conclusions are as follows:

(1) Through eigen-decomposition of the covariance matrix, the dominant spatial modes and their corresponding temporal coordinates were effectively extracted. This allows for the characterization of the complex wind pressure field using a limited number of modes with clear physical meanings.

(2) The energy distribution exhibits a "dispersed" feature rather than being concentrated in the first few modes. While the first mode accounts for 32.41% of the total energy, the 90% energy threshold is not reached

until the 18th mode. This relatively slow decay rate is a physical indicator of the multi-scale turbulent interactions and intense flow separation inherent to the asymmetric 2:1 aspect ratio canopy.

(3) Reconstruction analysis at the critical windward corner (Point 1)—the region characterized by the most intense flow separation and highest turbulence—verifies the robustness of the POD-based reduced-order model. Utilizing only the first three modes (r=3), the reconstructed signal $\hat{p}(t)$ achieves high-fidelity agreement with the original data, yielding an (RMSE) of 0.1105 and an *NRMSE* of 6.18%. These metrics demonstrate that the framework effectively captures dominant aerodynamic features and peak suction characteristics even in highly stochastic flow regions, proving the feasibility of high-ratio data compression for structural monitoring.

(4) The methodology established in this study provides a foundational framework for addressing broader problems in aerospace aero-thermo-fluid systems. The ability to extract primary features from complex separation flows is directly applicable to predicting unsteady aerodynamic loads, buffeting effects, and panel/skin pressure fluctuations in aircraft components. Furthermore, this reduced-order modeling approach can be extended to real-time structural health monitoring and the suppression of flow-induced vibrations (FIV) in high-performance aerospace structures.

DECLARATION OF COMPETING INTEREST

The authors declared no potential conflicts of interest with respect to the research, authorship, or publication of this article.

ACKNOWLEDGMENTS

This study was supported by the National Key R&D Program of China under Grant No. 2022YFB2602700, the National Natural Science Foundation of China (Grant No.52378216), the Chongqing Natural Science Foundation for Outstanding Young Scientists Fund (Grant No. CSTB2024NSCQ-JQX0027), and the Support Plan for Returned Overseas Scholars of Chongqing (cx2024004).

Additionally, we would like to express our sincere gratitude to Professor Yukio Tamura for generously sharing the experimental data that were essential to the implementation and validation of this study.

REFERENCES

[1] Mostafa K, Zisis I, Stathopoulos T. Codification of wind loads on hip roof overhangs of low-rise buildings[J]. Engineering Structures, 2023, 288: 116199. https://doi.org/10.1016/j.engstruct.2023.116199

[2] Wang J, Wang F, Chen X, *et al*. Investigation of wind load characteristics of cantilevered scaffolding of a high-rise building based on field measurement[J]. Energy and Buildings, 2025, 328: 115123. https://doi.org/10.1016/j.enbuild.2024.115123

[3] Sun W, Zhang Q. Universal equivalent static wind loads of fluctuating wind loads on large-span roofs based on compensation of structural frequencies and modes[C]//Structures. Elsevier, 2020, 26: 92-104. https://doi.org/10.1016/j.istruc.2020.04.008

[4] Zhang B, Nie S, Liu M, *et al*. Experimental Study on Wind Load of Large-Span Flexible Photovoltaic Structure Considering Different Tilt Angles[J]. Energies, 2025, 18(18): 4820. https://doi.org/10.3390/en18184820

[5] Ma T, Zhao L, Ji T, *et al*. Case study of wind-induced performance and equivalent static wind loads of large-span openable truss structures[J]. Thin-Walled Structures, 2022, 175: 109206. https://doi.org/10.1016/j.tws.2022.109206

[6] Hao Y, Han T, Wu H, *et al*. Study on the Wind-induced Interference Effect of a Large-span Roof Structure Building Group[J]. KSCE Journal of Civil Engineering, 2024, 28(4): 1392-1410. https://doi.org/10.1007/s12205-024-1356-1

[7] Kim Y C, Shan W, Yang Q S, *et al*. Effect of panel shapes on wind-induced vibrations of solar wing system under various wind environments[J]. Journal of Structural Engineering, 2020, 146(6): 04020104. https://doi.org/10.1061/(ASCE)ST.1943-541X.0002642

[8] Huang D, Chen G. Wind pressure distribution, non-Gaussian characteristics, and conical vortices of a large-span roof with variable arc angles[J]. Journal of Building Engineering, 2022, 57: 104929. https://doi.org/10.1016/j.jobe.2022.104929

[9] Wu Y, Zhang W, Miao P, *et al*. Wind-induced interference effect of complex building clusters on long-span roof structures[J]. Journal of Fluids and Structures, 2024, 129: 104157. https://doi.org/10.1016/j.jfluidstructs.2024.104157

[10] Jia H, Dang H, Ma Q, *et al*. Airflow Patterns around Obstacles with Large-Span Shallow Shell Roof: Wind Tunnel Measurements and Direct Simulation[J]. Mathematical Problems in Engineering, 2019, 2019(1): 9619282. https://doi.org/10.1155/2019/9619282

[11] Behera S, Ghosh D, Mittal A K, *et al*. The effect of plan ratios on wind interference of two tall buildings[J]. The Structural Design of Tall and Special Buildings, 2020, 29(1): e1680. https://doi.org/10.1002/tal.1680

[12] Tamura Y, Xu X, Yang Q. Characteristics of pedestrian-level Mean wind speed around square buildings: Effects of height, width, size and approaching flow profile[J]. Journal of Wind Engineering and Industrial Aerodynamics, 2019, 192: 74-87. https://doi.org/10.1016/j.jweia.2019.06.017

[13] Heidt L, Colonius T. Spectral proper orthogonal decomposition of harmonically forced turbulent flows[J]. Journal of fluid mechanics, 2024, 985: A42. https://doi.org/10.1017/jfm.2024.70

[14] Nekkanti A, Schmidt O T. Gappy spectral proper orthogonal decomposition[J]. Journal of Computational Physics, 2023, 478: 111950. https://doi.org/10.1016/j.jcp.2023.111950

[15] Olesen P J, Hodžić A, Andersen S J, *et al*. Dissipation-optimized proper orthogonal decomposition[J]. Physics of Fluids, 2023, 35(1). https://doi.org/10.1063/5.0131923

[16] Tamura Y, Ueda H, Kikuchi H, *et al*. Proper orthogonal decomposition study of approach wind-building pressure correlation[J]. Journal of wind engineering and industrial aerodynamics, 1997, 72: 421-431. https://doi.org/10.1016/S0167-6105(97)00270-5

[17] Tamura Y, Suganuma S, Kikuchi H, *et al*. Proper orthogonal decomposition of random wind pressure field[J]. Journal of fluids and structures, 1999, 13(7-8): 1069-1095. https://doi.org/10.1006/jfls.1999.0242

[18] Kim B, Tse K T. POD analysis of aerodynamic correlations and wind-induced responses of two tall linked buildings[J]. Engineering Structures, 2018, 176: 369-384. https://doi.org/10.1016/j.engstruct.2018.09.013

[19] Zhou L, Tse K T, Hu G. Experimental investigation on the aerodynamic characteristics of a tall building subjected to twisted wind[J]. Journal of Wind Engineering and Industrial Aerodynamics, 2022, 224: 104976. https://doi.org/10.1016/j.jweia.2022.104976

[20] Yuan K, Chen Z, Xu Y, *et al*. Aerodynamic interference and flow field mechanisms of three-dimensional tandem square cylinders based on proper orthogonal decomposition and high-order dynamic mode decomposition modeling[J]. Physics of Fluids, 2025, 37(5). https://doi.org/10.1063/5.0270219

https://doi.org/10.66000/3110-9780.2026.02.01